

1 **Smooth crustal velocity models cause a depletion of high-frequency ground**  
2 **motions on soil in 2-D dynamic rupture simulations**

3  
4 **Yihe Huang<sup>1</sup>**

5 <sup>1</sup>Department of Earth and Environmental Sciences, University of Michigan.

6 Corresponding author: Yihe Huang ([yiheh@umich.edu](mailto:yiheh@umich.edu))  
7

8  
9 This paper is a preprint submitted to EarthArXiv. It is under review in the Bulletin of the  
10 Seismological Society of America (BSSA). Please feel free to contact the author if you have any  
11 feedback.  
12  
13  
14  
15  
16  
17  
18  
19  
20  
21  
22  
23  
24  
25  
26  
27  
28  
29  
30  
31

32  
33  
34  
35  
36  
37  
38  
39  
40  
41  
42  
43  
44  
45  
46  
47  
48  
49  
50  
51  
52  
53  
54  
55  
56  
57  
58  
59  
60  
61  
62

**Abstract**

A depletion of high-frequency ground motions on soil sites has been observed in recent large earthquakes and is often attributed to a nonlinear soil response. Here we show that the reduced amplitudes of high-frequency horizontal-to-vertical spectral ratios on soil can also be caused by a smooth crustal velocity model with low shear wave velocities underneath soil sites. We calculate near-fault ground motions using both 2-D dynamic rupture simulations and point-source models for both rock and soil sites. The 1-D velocity models used in the simulations are derived from empirical relationships between seismic wave velocities and depths in northern California. The simulations for soil sites feature lower shear wave velocities and thus larger Poisson’s ratios at shallow depths than those for rock sites. The lower shear wave velocities cause slower shallow rupture and smaller shallow slip, but both soil and rock simulations have similar rupture speeds and slip for the rest of the fault. However, the simulated near-fault ground motions on soil and rock sites have distinct features. Compared to ground motions on rock, horizontal ground acceleration on soil is only amplified at low frequencies, whereas vertical ground acceleration is de-amplified for the whole frequency range. Thus, the horizontal-to-vertical spectral ratios on soil exhibit a depletion of high-frequency energy. The comparison between smooth and layered velocity models demonstrates that the smoothness of the velocity model plays a critical role in the contrasting behaviors of horizontal-to-vertical spectral ratios on soil and rock for different rupture styles and velocity profiles. Our results reveal the significant role of shallow crustal velocity structure in the generation of high-frequency ground motions on soil sites.

63  
64  
65  
66  
67  
68  
69  
70  
71  
72  
73  
74  
75  
76  
77  
78  
79  
80  
81  
82  
83  
84  
85  
86  
87  
88  
89  
90  
91  
92

## Introduction

It is well known that near-surface site effects significantly contribute to strong ground motions from earthquakes. In particular, sedimentary basins or soil sites are common in seismically active regions and are often considered to amplify ground motions due to seismic wave reverberations. However, especially for large earthquakes, the amplification of ground motions seems to strongly depend on wave frequencies. For example, in the 2019  $M_W$  7.1 Ridgecrest earthquake, the amplitudes of horizontal-to-vertical spectral ratios (HVSRS) at deep alluvium sites are much lower than those at thin alluvium and rock sites for frequencies higher than 3 Hz (Hough et al., 2020). A similar depletion of high-frequency energy on soil sites has been shown for the 1985  $M_W$  8.0 Michoacan, Mexico earthquake, 1989  $M_W$  6.9 Loma Prieta, California earthquake (Beresnev and Wen, 1996), 1994  $M_W$  6.7 Northridge, California earthquake (Field et al., 1997), the 2015  $M_W$  7.8 Gorkha, Nepal, earthquake (Dixit et al., 2015), and the 2016  $M_W$  5.9 Southeast Off-Mie, Japan, earthquake (Kubo et al., 2019). Such characteristics of high-frequency ground motions are usually attributed to the nonlinear soil response associated with an increase in damping and a reduction in shear modulus for large shear strain (Beresnev and Wen, 1996). It is worth noting that low-rise buildings on soil sites may experience less damage due to the significant reduction of high-frequency ground motions (Trifunac and Todorovska, 1998).

However, it is still unclear how properties of near-surface materials, including seismic wave velocities, Poisson's ratio, and attenuation parameters, contribute to the variability in site responses to seismic waves and whether the velocity structure underneath soil sites may cause the depletion of high-frequency energy in HVSRS. The classification of near-surface site conditions is primarily based on the time-averaged shear wave velocity of the top 30 m of the crust (Park and Elrick, 1998),  $V_{S30}$ , which is shown to correlate with geologic units in California (Wills et al., 2000) and ground motion amplification (Field, 2000). For broad site-classifications used by National Earthquake Hazards Reduction Program (NEHRP), rock sites should have  $V_{S30}$  larger than 760 m/s, whereas soil sites can be further classified to soft soil (site class E,  $V_{S30} \leq$

93 180 m/s), stiff soil (site class D,  $180 < V_{S30} \leq 360$  m/s), and very dense soil (site class C,  
94  $360 < V_{S30} \leq 760$  m/s) (BSSC, 2001).

95

96 The low  $V_{S30}$  of soil sites leads to Poisson's ratios considerably larger than 0.25, the value for a  
97 perfectly isotropic elastic material, since the compressional wave velocity ( $V_p$ ) is not reduced at  
98 the same rate as the shear wave velocity ( $V_s$ ) for shallow depths. Brocher (2005) compiled  $V_p$   
99 and  $V_s$  from borehole logs, vertical seismic profiles, laboratory measurements, and tomography  
100 studies for a variety of rocks, primarily in California. The data shows that  $V_s$  varies more rapidly  
101 with  $V_p$  when  $V_p$  is less than 3.75 km/s, resulting in Poisson's ratios between 0.25 and 0.5 in the  
102 shallow crust (e.g., top 1-2 km). Especially for young, saturated sediments, the Poisson's ratio  
103 approaches 0.5 as  $V_s$  quickly drops to 100 m/s when  $V_p$  is reduced to 1500 m/s. Based on the  
104 empirical relationship between  $V_p$  and  $V_s$  (equation (9) in Brocher, 2005), soil sites with  $V_{S30}$   
105 less than 760 m/s should have Poisson's ratios larger than 0.43. Taking into consideration large  
106 Poisson's ratios at shallow depths can help improve the stability of hypocenter determination  
107 (Nicholson and Simpson, 1985).

108

109 Another factor that can strongly affect ground motions is seismic wave attenuation of near-  
110 surface materials, quantified by the Q values. Based on the borehole data of local earthquakes in  
111 California, Abercrombie (1997) showed that over 90% of the attenuation occurs within the upper  
112 3 km, and the near-surface Q is very low (i.e.,  $Q_p \sim 26$  and  $Q_s \sim 15$  in the upper 300 m). The study  
113 concluded that the near-surface attenuation has a weak dependence on site conditions, as Q is  
114 more sensitive to fracture density, temperature and fluid content rather than rock types. Other  
115 studies (e.g., Bethmann, 2012; Edwards and Fah, 2013; Wang, 2016) also found similar  
116 attenuation parameters for soil and rock sites in Europe, Middle East and Asia. However, the 3-D  
117 attenuation models of the southern California crust reveal low  $Q_p$  and  $Q_s$  values in the top 1 km  
118 layer of major sedimentary basins and high Q zones that correspond to the high-velocity rocks of  
119 the mountain ranges (Hauksson and Shearer, 2006). Van Houtte et al. (2011) also validated the  
120 correlation between  $V_{S30}$  and the high-frequency decay parameter  $\kappa$  using ground motion data  
121 from both the Kiban-Kyoshin network (KiK-net) in Japan and the Next Generation Attenuation  
122 of Ground Motions (NGA) database. Neighbors et al. (2015) showed that  $\kappa$  estimated from the  
123 2010 Maule, Chile aftershocks exhibits site-condition dependence, but the overlap of error bars

124 of attenuation parameter measurements suggests the difference between hard rock and soil sites  
125 may be insignificant.

126

127 The observed low  $V_s$ , large Poisson's ratio, and possible low  $Q_s$  of soil sites encourage the  
128 hypothesis that they may partially contribute to the features of high-frequency ground motions.  
129 3D velocity models with low  $V_s$  and large Poisson's ratios for soil sites are commonly  
130 implemented in kinematic ground motion simulations (e.g., Olsen, 2000; Frankel, 2009;  
131 Aagaard, 2010; Taborda and Bielak, 2014; Asano, 2016; Pitarka, 2016; Rodgers, 2018), though  
132 there is still a limitation in the lowest  $V_s$  that can be resolved. However, due to the lack of  
133 observational constraints or for computational convenience, ground motion simulations may also  
134 assume a constant Poisson's ratio inside the sedimentary basin that is much lower than observed  
135 values (e.g., Meza-Fajardo, 2016) or velocity models with a few layers. Some kinematic ground  
136 motion simulations also explicitly consider the reduction of stiffness during nonlinear soil  
137 deformation by correcting site responses (e.g., Esmailzadeh et al., 2019; Rodgers et al., 2020).

138

139 Motivated by the contrasting behaviors of HVSRs on soil and rock sites in the 2019  $M_W$  7.1  
140 Ridgecrest earthquake (Hough et al., 2020), we characterize the contributions of shallow velocity  
141 structure to the differences of ground motion amplitudes, frequency contents and HVSRs on soil  
142 and rock sites by simulating 2-D dynamic rupture propagating on a vertical 1-D fault. Dynamic  
143 rupture simulations calculate kinematic rupture processes of earthquakes by respecting fault  
144 physics and considering the interaction between fault stress and frictional strength as well as  
145 seismic wave propagation in the surrounding medium, leading to realistic scenarios of strong  
146 ground motions (e.g., Harris et al., 2018). Using dynamic rupture simulations helps differentiate  
147 the respective contributions of earthquake source and seismic wave propagation, which are both  
148 affected by the velocity structure and attenuation parameter. In the Methodology section, we  
149 discuss the velocity model, attenuation parameters, stresses and frictional parameters used in our  
150 dynamic rupture simulations. In the Results section, we present the source characteristics of  
151 simulated rupture (e.g., slip, slip rate and rupture speed), and compare the acceleration  
152 waveforms and HVSRs recorded on soil and rock sites. We show that a smooth velocity model  
153 combined with low  $V_s$  can give rise to diminished amplitudes of high-frequency HVSRs in soil  
154 simulations.

155

## 156 **Methodology**

157

158 In both 2-D dynamic rupture simulations and point-source models, we use a 1-D velocity model  
159 derived from empirical relationships between seismic wave velocities and depths in northern  
160 California (Brocher, 2008). Since Holocene and Plio-Quaternary deposits can greatly amplify  
161 ground motions in northern California, we adopt the depth variations of seismic wave velocities  
162 for Holocene and Plio-Quaternary sedimentary rocks at depths less than 500 m and for older  
163 Cenozoic sedimentary rocks at depths more than 500 m (Table 1; Figure 1a). Since the maximum  
164 resolvable frequency of ground motions is determined by the slowest seismic wave velocity in  
165 the simulations,  $V_p$  and  $V_s$  in the top 60 m are kept constant and equal to the values at 60 m  
166 depth to resolve ground motions at high frequencies. Given  $V_{S30}=436$  m/s, the site condition is  
167 classified as a very dense soil. We refer to this velocity model as model S (“S” stands for soil)  
168 for the rest of the paper. The Poisson’s ratio in model S can be calculated from  $\frac{(V_p/V_s)^2-2}{2(V_p/V_s)^2-2}$  using  
169  $V_p$  and  $V_s$  in Table 1. To compare ground motions recorded at soil and rock sites, we use a  
170 different 1-D velocity model based on the same  $V_p$  vs. depth relationship, but with a Poisson’s  
171 ratio of 0.25. Hence,  $V_{S30}=988$  m/s in this velocity model, and the site condition is classified as a  
172 rock site. We refer to this velocity model as model R (“R” stands for rock) for the rest of the  
173 paper. The major difference between velocity models S and R is at depths shallower than 3 km,  
174 where  $V_s$  is significantly lower in model S (dashed and dotted lines in Figure 1a).

175

176 We calculate density from  $V_p$  using the Nafe-Drake curve (Brocher, 2005; Ludwig et al., 1970).  
177 We estimate  $Q_s$  from  $V_s$  using the relationship ( $Q_s = -16 + 104.13V_s - 25.225V_s^2 + 8.2184V_s^3$   
178 for  $0.3 \text{ km/s} < V_s < 5 \text{ km/s}$ ) constrained by the forward modeling of strong ground motions  
179 from the 1994 Northridge earthquake (Brocher, 2008; Graves and Pitarka, 2004).  $Q_p$  is assumed  
180 to be twice the value of  $Q_s$  (Brocher, 2008). Similar to seismic wave velocities,  $Q_p$  and  $Q_s$  are  
181 kept constant in the top 60 m ( $Q_p=50$  and  $Q_s=25$ ). We also investigate the effects of the same  
182 attenuation profiles for soil and rock simulations in the Results section, given the possible weak-  
183 dependence of near-surface attenuation on site conditions (Abercrombie, 1997; Bethmann,  
184 2012; Edwards and Fah, 2013; Wang, 2016).

185

186 We simulate along-dip rupture propagation as mode II rupture on a 1-D vertical fault governed  
187 by a linear slip-weakening friction law (Ida, 1972; Andrews, 1976a), which describes the drop of  
188 friction coefficient from the static level  $\mu_s$  to the dynamic level  $\mu_d$  when slip reaches the critical  
189 slip distance,  $D_c$  (Figure 1b). A free surface is applied to the top boundary of the modeling  
190 domain, whereas the other boundaries are absorbing boundaries (Clayton and Engquist, 1977).  
191 Synthetic waveforms are calculated on the surface at distances of 5, 10 and 15 km from the fault.  
192 The station-fault distances are chosen to be similar to those in the ground motion analysis of the  
193 2019 Ridgecrest earthquake (Hough et al., 2020).

194

195 Frictional parameters and fault stresses vary along depth in our simulations. Both  $\mu_d$  and  $D_c$  are  
196 constant at seismogenic depths (5-18 km), but increase at shallower and deeper parts to allow  
197 earthquake rupture to stop (Figure 1b). Note that using  $D_c = 1m$  at shallow depths does not have  
198 a significant impact on the resulting earthquake rupture and ground motions at the distances  
199 considered in this study (i.e., 5-15 km), but the choice of  $D_c$  can have a large effect on ground  
200 motions at distances closer to the fault (e.g., Wang et al., 2019). Effective normal stress  $\sigma_o$   
201 increases linearly with depth for the first 3 km and remains a constant value of 50 MPa for the  
202 rest of the fault (Figure 1c). Initial shear stress  $\tau_o$  follows the variation of effective normal stress  
203 except inside the nucleation zone to keep an S ratio of 2 ( $S = \frac{\mu_s \sigma_o - \tau_o}{\tau_o - \mu_d \sigma_o}$ ). Dynamic rupture is  
204 nucleated at a depth of 10 km by a 2 km long overstressed patch with the initial shear stress  $\tau_o$   
205 0.3% higher than the static shear strength  $\mu_s \sigma_o$ . As rupture propagates, seismic waves are  
206 radiated into the surrounding medium, which generates ground motions.

207

208 Dynamic rupture is solved numerically using a spectral element method (SEM2DPACK,  
209 Ampuero, 2009). We require at least 5 GLL nodes in the process zone to resolve the reduction  
210 from the static friction to dynamic friction during rupture propagation. To resolve ground motions  
211 at a maximum frequency of 6 Hz, we use a 75-m element mesh with 5 GLL nodes, so there are at  
212 least 5 nodes for the minimum wavelength in the simulations. The resolution test shows that in  
213 fact ground motions can be resolved to a maximum frequency of 7-8 Hz for the 75-m element.  
214 Thus, our results are shown up to a maximum frequency of 7 Hz. We allow frequency-independent  
215 seismic attenuation in the simulations by adding viscoelastic terms in the stress-strain relations

216 (Moczo et al., 2004). Three anelastic functions and relaxation frequencies are used to produce an  
217 approximately flat  $Q$  between 0.1 and 10 Hz. The details of the implementation of attenuation in  
218 dynamic rupture simulations are shown by Huang et al. (2014). For frequencies higher than 1 Hz,  
219  $Q$  can be an increasing function of frequency and is modeled in the form of a power law (Withers  
220 et al., 2015), though the frequency-dependence of  $Q$  may affect ground motions on soil and rock  
221 sites in a similar fashion.

222

## 223 **Results**

224

225 In this section, we present dynamic rupture scenarios and resulting ground accelerations for soil  
226 and rock simulations that have different velocity models and attenuation parameters. We discuss  
227 in more detail how the velocity models and attenuation parameters can change the variation of  
228 horizontal-to-vertical spectral ratios and address why a depletion of high-frequency energy is  
229 observed on soil. We also show how rupture styles (buried vs. surface rupture), double-couple  
230 point sources and velocity structure details at shallow depth affect ground motions on soil and  
231 rock sites.

232

### 233 *Dynamic rupture simulations*

234

235 The values of fault friction and stresses in our simulations allow dynamic rupture to propagate at  
236 nearly the Rayleigh wave speed in both up-dip and down-dip directions shortly after nucleation  
237 (Figures 2a and b). Different velocity models have a negligible effect on rupture speed, slip and  
238 slip rate for depths larger than 3 km. The largest final slip is  $\sim 11$  m near the hypocenter depth (10  
239 km). If we define the along-dip rupture width as the region where slip is greater than 1 % of the  
240 maximum final slip, then the rupture width is  $\sim 24$  km in both models. Assuming that the rupture  
241 length is equal to the rupture width and slip at a given depth is the same along strike, simulated  
242 rupture generates earthquakes of magnitude  $\sim 7.3$  for both model S and model R. Note that the  
243 magnitude calculated from the 2-D model is larger than the magnitude of a real earthquake with  
244 the same rupture area and peak slip, since the peak slip is assumed to extend along strike in our  
245 magnitude calculation.

246



247 At shallow depths, however, model S and model R exhibit different earthquake source  
248 properties. Rupture becomes significantly slower as it propagates through the shallow part of the  
249 fault for model S and results in smaller slip due to lower  $V_s$ . A detailed inspection of final slip  
250 shows that surface slip is only one-third of that for model R, and slip at 1 km depth is about two-  
251 thirds of that for model R. The difference in final slip gradually decreases with depth (Figure 2c).  
252 Moreover, slip rate functions have multiple fluctuations and contain a mixture of sharp and  
253 smooth slip pulses for both models (Figure 2d). The spatiotemporal slip rate distribution (Figures  
254 3a and b) reveals that the sharp slip pulse, a most noticeable feature in the slip rate function at  
255 shallow depths, originates from the surface S-wave reflection. Hence, sharp pulses appear earlier  
256 in slip rate functions of model R given its higher  $V_s$  at shallow depths. The smooth pulse  
257 following behind the sharp pulse has a larger average slip rate at shallow depths in model R, and  
258 rise time (i.e, the duration of slip rate function) is longer especially for depths shallower than 1  
259 km. Together these two effects contribute to a larger shallow slip in model R.

260

### 261 *Seismic acceleration waveform and spectra*

262

263 The previous section shows that the lower  $V_s$  in model S results in smaller slip and slower  
264 rupture speed at the shallow part of the fault, but the overall characteristics of rupture  
265 propagation are very similar between the two models at depths larger 3 km, where most seismic  
266 energy is radiated. Near-fault ground motions from these two rupture scenarios, however, exhibit  
267 distinct features, suggesting that different velocity models have a more significant influence on  
268 the propagation of seismic waves to near-fault stations. This important role of velocity models is  
269 further validated in sections “Buried rupture vs. surface rupture” and “Point-source models of  
270 ground motions on soil and rock sites” for which rupture properties are either very similar  
271 throughout the fault or the same for different models. Figure 3 demonstrates ground acceleration  
272 recorded at a distance of 10 km from the fault. Both horizontal and vertical acceleration last for a  
273 longer duration on soil than on rock. Peak horizontal acceleration on soil is slightly larger than  
274 on rock, whereas peak vertical acceleration on soil is slightly lower. Vertical acceleration  
275 waveforms on soil and rock also have distinct characteristics. Vertical acceleration on soil stays  
276 at low amplitudes after the P-wave arrival, while vertical acceleration on rock has multiple large-  
277 amplitude peaks with the largest peak arriving at  $\sim 13$ s after the P-wave arrival.

278

279 To understand the frequency-dependence of near-field ground motions, we calculate acceleration  
280 spectra by taking a Fourier transform of the 45 s acceleration records (Figure 3e). The spectra are  
281 smoothed using a 30-point moving average. For soil sites, we find spectral amplitudes of  
282 horizontal acceleration are considerably larger than those of vertical acceleration for the whole  
283 frequency band of interest (0.7-7 Hz). For rock sites, spectral amplitudes of horizontal  
284 acceleration are, on average, slightly larger than those of vertical acceleration at frequencies less  
285 than 1 Hz and higher than 4 Hz. Spectral amplitudes of horizontal and vertical components on  
286 rock become indistinguishable at 1-4 Hz.

287

288 Comparing horizontal acceleration spectra recorded by soil and rock sites, we find soil sites  
289 amplify near-field horizontal ground acceleration only at low frequencies. The horizontal  
290 spectral amplitude on soil is higher by about a factor of 1.7 at 0.7 Hz than on rock. At  
291 frequencies higher than 1.1 Hz, there is no significant difference between the soil and rock sites  
292 in horizontal spectral amplitudes, which agrees qualitatively with the finding by Joyner and  
293 Boore (1988). They suggested that similar horizontal high-frequency acceleration amplitudes for  
294 soil and rock sites can result from the suppression of high-frequency amplification by attenuation  
295 in the soil. However, our rupture simulations in a purely elastic medium, in which attenuation  
296 effects are not considered, still show similar horizontal acceleration amplitudes at higher  
297 frequencies for soil and rock sites (dotted and dash-dot lines in Figure 3e).

298

### 299 *Horizontal-to-vertical spectral ratios (HVSRS)*

300

301 We then calculate HVSRS for stations at distances of 5, 10 and 15 km on soil and rock sites  
302 (Figure 4). To further investigate the effects of attenuation parameters, we also simulate ground  
303 motions from a rock model with the same attenuation parameters as the soil model (dashed lines  
304 in Figure 4), i.e., smaller  $Q_p$  and  $Q_s$  at shallow depths than the previous rock model. However,  
305 we find the difference between HVSRS on soil and rock sites has a weak dependence on  
306 attenuation parameters. Overall, HVSRS on soil are higher than those on rock at low frequencies.  
307 For the station at 5 km from the fault, HVSRS on soil approach those on rock at frequencies  
308 higher than 3 Hz. For the station at 10 km from the fault, HVSRS on soil become lower than

309 those on rock at frequencies higher than 6 Hz. HVSRs on soil also share similar features at  
310 different stations: Their amplitudes are the largest at  $\sim 1$  Hz and gradually decrease at higher  
311 frequencies. For the station at 10 km from the fault, HVSRs on soil are higher by a factor of  $\sim 3$   
312 at 1 Hz and by a factor of  $\sim 2$  at 3 Hz than on rock.

313

314 To investigate the frequency-dependence of HVSRs, we normalize them by the maximum  
315 amplitudes for the frequency band of interest. The normalized HVSRs clearly show that high-  
316 frequency content is relatively richer on rock than on soil (Figure 4). This simulation result is  
317 qualitatively similar to the observed reduced amplitudes of high-frequency HVSRs at deep  
318 alluvium sites for the recent Ridgecrest earthquake (Hough et al., 2020). It is worth noting that  
319 for the stations at 10 and 15 km distances, HVSRs on rock do not decay at high frequencies as  
320 observed in real data, but rather slightly increase in amplitudes. An even steeper increase in  
321 HVSRs at high frequencies may be observed in simulations if  $Q$  is modeled as an increasing  
322 function of frequency (Withers et al., 2015). As discussed later, reproducing the exact behaviors  
323 of high-frequency HVSRs may require 3D rupture simulations or small-scale velocity  
324 heterogeneity that can generate more scattering of seismic waves.

325

### 326 *What causes the depletion of high-frequency energy on soil?*

327

328 Our analysis shows that low  $V_s$  and large Poisson's ratio of the shallow crust contribute to the  
329 amplification of low-frequency horizontal ground motions on soil, but it is intriguing why high-  
330 frequency horizontal ground motions are not similarly amplified as their low-frequency  
331 counterparts. The attenuation effect does not seem to play a role, as elastic simulations also  
332 produce similar horizontal acceleration amplitudes on soil and rock at higher frequencies (dotted  
333 and dash-dot lines in Figure 3e). Besides the difference in  $V_s$ , the velocity models in our  
334 simulations have smooth velocity gradients, governed by the empirical relationships between  
335 seismic wave velocities and depths (Brocher, 2008). We hypothesize that a smooth velocity  
336 gradient may not be as efficient as a 1-D layer model in amplifying high-frequency energy, since  
337 the velocity change within the wavelength that corresponds to a given high frequency would be  
338 small for a smooth velocity gradient.

339

340 To test this hypothesis, we generate two 1-D layer models with seismic velocities directly  
341 derived from the smooth velocity gradient (Figure 5). In the first model, we use 16 layers to  
342 closely mimic the smooth velocity gradient. In the second model, we define 5 velocity layers  
343 with the same boundaries (i.e., 0.5, 4, 7 and 12 km) used by Brocher (2008) to derive the  
344 empirical relationships. We then represent the seismic velocity for each layer using the median  
345 seismic velocity. The density and attenuation parameters are derived in the same way. We find  
346 that HVSRs on soil still decay at high frequencies for the 16-layer velocity model, and the  
347 contrasting behaviors of soil and rock sites are similar to the smooth velocity model. For the 5-  
348 layer velocity model, however, HVSRs on soil do not show a clear decay as frequency increases  
349 and have comparable amplitudes at low and high frequencies. The different outcomes of the 1-D  
350 layer models suggest that a smooth velocity gradient or a velocity model with sufficient layers to  
351 mimic a smooth velocity gradient plays a critical role in the depletion of high-frequency energy  
352 on soil in our simulations.

353

#### 354 *Buried rupture vs. surface rupture*

355

356 Fault stress and frictional conditions in previous simulations allow rupture to reach the surface.  
357 Ground motion observations suggest that surface rupture and buried rupture can have a strong  
358 influence on the characteristics of ground motions. For example, ground motions generated by  
359 surface rupture are weaker than buried rupture for a period range of 0.3-3 sec (Somerville, 2003).  
360 Such difference in ground motions can be attributed to a shallow weak zone as well as the larger  
361 stress drop and deeper hypocenter of buried rupture (Pitarka, et al., 2009). Here we investigate  
362 how buried rupture influences the observed acceleration waveform and spectral features. The  
363 comparison between surface rupture and buried rupture also helps us understand how rupture  
364 propagation in the shallow crust affects the ground motion difference between soil and rock sites.

365

366 To simulate buried rupture, we increase  $\sigma_o$ ,  $\mu_d$  and  $D_c$  in the top 3 km to values that prevent  
367 rupture from reaching the surface for both velocity models. The buried rupture models have  
368 similar rupture properties at shallow depths. The resulting slip is less than 0.2 m for the top ~ 1  
369 km and is zero near the surface. Magnitudes of simulated earthquakes are ~7.2, slightly smaller  
370 than the surface-rupturing scenarios. Near-source acceleration records of buried rupture show

371 similar waveform features to surface rupture for the first 10 s after the P-wave arrival (Figure 6),  
372 but wave reverberations afterwards seem to be less pronounced on both soil and rock for buried  
373 rupture. On soil sites, since the lack of wave reverberations affects the apparent total duration of  
374 ground motions, spectral amplitudes of horizontal and vertical acceleration are slightly reduced  
375 at 0.7 Hz (Figure 6). On rock sites, the lack of wave reverberations after the first 10 s has  
376 significantly reduced ground motions, especially for the vertical component. Note that the peak  
377 vertical acceleration on rock arrives at 13 s after the P-wave arrival for surface rupture (Figure  
378 3). Compared to surface rupture, spectral amplitudes of vertical acceleration on rock are reduced  
379 by almost a half for buried rupture (Figure 6). As a result, the HVSRs on rock are also larger for  
380 buried rupture (Figure 7).

381  
382 The larger HVSRs for buried rupture (Figure 7), however, do not affect previous results  
383 regarding the difference of HVSRs on soil and rock. The results from buried rupture confirm the  
384 finding that different velocity models, rather than rupture processes, have a major influence on  
385 the contrasting behaviors of ground motions on soil and rock. For the station at 5 km distance,  
386 HVSRs on soil and rock are both increased by a factor of  $\sim 2$  for buried rupture compared to the  
387 values for surface rupture at low frequencies. Thus, HVSRs on soil are still higher by a factor of  
388 2-3 for frequencies around 0.7 Hz. For the station at 10 km distance, HVSRs on soil are higher  
389 by a factor of  $\sim 2$  than on rock for frequencies around 1 Hz. Normalized HVSRs also support  
390 richer high-frequency energy on rock than on soil (Figure 7). The contrast between normalized  
391 soil and rock HVSRs at 5 km distance is even larger for buried rupture than for surface rupture,  
392 especially for frequencies higher than 1.5 Hz.

393

#### 394 *Point-source models of ground motions on soil and rock sites*

395

396 Our dynamic rupture simulations have demonstrated that different velocity structures underneath  
397 soil and rock sites have a critical impact on high-frequency ground motions. Here we show that  
398 the contrasts of HVSRs on soil and rock sites can also be observed in point-source models, in  
399 which the earthquake is represented by a double-couple source with a dip angle of  $90^\circ$  and a  
400 Gaussian source time function. The central frequency of the source time function is 1 Hz, which

401 is near the corner frequencies of  $M_w \sim 5$  earthquakes. The source properties of earthquakes are  
402 the same for both soil and rock models.

403

404 Similar to dynamic rupture results, the simulated HVSRs on soil sites are significantly larger  
405 than those on rock sites at low frequencies (Figure 8). The difference of HVSRs on rock and soil  
406 sites is especially large at 1-2 Hz for all the stations. HVSRs on soil gradually decay and  
407 approach those on rock at high frequencies. The normalized HVSRs also support richer high-  
408 frequency content in HVSRs on rock sites, though the HVSRs calculated from a point source  
409 appear to have a bump around 3 Hz for rock sites. Given the same earthquake source properties  
410 in point-source models, they demonstrate that the amplified low-frequency HVSRs and the rapid  
411 decay of HVSRs at high frequencies on soil sites are primarily the result of the smooth velocity  
412 structure.

413

#### 414 *Velocity models for the top 60 m*

415

416 One remaining question in our dynamic rupture simulations is the effect of the velocity structure  
417 for the top 60 m. In previous simulations, seismic velocities are kept constant at this depth range  
418 to accurately calculate ground motions at a maximum frequency of 7 Hz with reasonable  
419 computational costs. In this section, we relax this particular model constraint and allow material  
420 properties to vary for the top 60 m.  $V_p$  and  $V_s$  are calculated from their depth variations for  
421 Holocene and Plio-Quaternary deposits at depths less than 60 m (Brocher, 2008). The density  
422 and attenuation parameters are also modified based on their relationships with seismic wave  
423 velocities.  $V_p$ ,  $V_s$ ,  $Q_p$  and  $Q_s$  are 700 m/s, 215 m/s, 26 and 13 at surface, respectively, in the soil  
424 model. Thus, the soil site falls into site class D rather than site class C in the previous models.  
425 Figure 9a illustrates the differences of seismic wave velocities and density between this velocity  
426 model and previous velocity model for soil sites. For a target maximum frequency of 3 Hz, there  
427 are at least 5 nodes for the minimum wavelength in the simulation.

428

429 The most noticeable feature of HVSRs resulting from this velocity model is an even faster decay  
430 of HVSRs on soil at high frequencies (Figure 9). HVSRs on soil are generally higher than those  
431 on rock at frequencies lower than 1 Hz and decrease to values less than 1 at  $\sim 1, 2$  and 3 Hz for

432 stations at 5, 10 and 15 km distances, respectively. HVSRs on soil become lower than those on  
433 rock at frequencies higher than  $\sim 2.5$  Hz. This interesting finding shows that the frequencies  
434 above which a depletion of high-frequency energy is observed in HVSRs also depends on the  
435 detailed velocity model at the shallowest depths.

436

## 437 **Discussion and Conclusions**

438

439 Our dynamic rupture simulations unveil the important contribution of velocity structure to the  
440 observed difference in ground motions on soil and rock sites. The low  $V_s$  and large Poisson's  
441 ratios in the top 3 km of the crust underneath soil sites, in combination with a smooth velocity  
442 gradient, amplify horizontal ground motions at low frequencies but reduce vertical ground  
443 motions for the whole frequency range. As a result, HVSRs on soil tend to exhibit larger  
444 amplitudes than on rock at low frequencies, but HVSRs on soil decay more rapidly than those on  
445 rock at high frequencies in our simulations.

446

447 The simulated HVSRs are in qualitative agreement with the observed average HVSRs at deep  
448 alluvium sites for the recent Ridgecrest earthquake (Hough et al., 2020). In the Ridgecrest  
449 observation, HVSRs at deep alluvium sites become lower than those on rock sites at frequencies  
450 above 3 Hz, which is observed in our simulations when material properties vary for the top 60 m  
451 (Figure 9), but not observed when  $V_s$  is kept constant at 460 m/s for the top 60 m. The better  
452 agreement between results from the velocity model with varying material properties for the top  
453 60 m and the Ridgecrest observation may be related to the fact that they both assume site class D  
454 for soil sites. However, it should also be noted that our dynamic rupture simulations are not  
455 designed to fully capture the rupture characteristics of the Ridgecrest earthquake given its 2-D  
456 nature. For example, the along-strike variation of rupture characteristics such as rupture  
457 directivity can modulate high-frequency ground motions. The exact behaviors of soil and rock  
458 sites can be affected by the azimuths of stations in 3-D simulations too. 3-D velocity models,  
459 especially those with the addition of small-scale material heterogeneity (Withers et al., 2019),  
460 can cause strong scattering of wave fields and more variability in ground motions. Though the 2-  
461 D rupture simulations may represent the contrasting behaviors of average HVSRs on soil and  
462 rock sites, future investigation should use a more realistic 3-D dynamic rupture simulation with a

463 full description of earthquake rupture and velocity model to reproduce the exact behaviors of  
464 observed HVSRs.

465  
466 A key point that needs to be emphasized is that the smooth velocity model used in this study  
467 applies to the crustal scale (i.e., the upper ~15 km), which is fundamental for regional ground  
468 motion simulations. However, the velocity structure for the top 100-200 m can have a significant  
469 influence on high-frequency ground motions too. It has been shown in 1-D site-response models  
470 that overly coarse velocity profiles for the top 100-200 m generate large strain localizations  
471 above impedance contrasts between adjacent layers, which can cause more dissipation of high-  
472 frequency energy (Kaklamanos and Bradley, 2018a; Kaklamanos et al., 2020). This effect is  
473 contrary to the effect of a coarse crustal velocity model in our 2-D dynamic rupture simulations  
474 (e.g., the 5-layer model in Figure 5). The variability of velocity profiles at very shallow depths  
475 should also be accounted for in future dynamic rupture models that simulate high-frequency  
476 ground motions.

477  
478 Our results have great implications for the understanding of near-field ground motions. The  
479 diminished high-frequency energy in ground motions on soil sites is usually interpreted as a  
480 result of nonlinear sediment response, which reduces high-frequency ground motions by  
481 increasing the damping of ground motions when shear strain increases (Bresnev and Wen, 1996).  
482 Our dynamic rupture simulations demonstrate that a smooth crustal velocity model with low  $V_s$   
483 underneath soil sites can cause different responses of horizontal and vertical ground motions and  
484 at least partially contribute to the depletion of high-frequency energy in the observed HVSRs.  
485 Some 3D ground motion simulations have considered smooth velocity profiles based on a certain  
486 relationship between seismic wave velocities and depths (e.g., Harmsen, 2008), and how high-  
487 frequency ground motions are influenced by smooth 3D velocity models in such simulations  
488 warrants further investigation. Our results support the development of high-resolution velocity  
489 models at shallow depths and provide new physical constraints that can be used to better inform  
490 ground motion simulations.

491  
492 **Data and Resources**

493



494 No data were used in this paper. Dynamic rupture is solved using a modified version of  
495 SEM2DPACK (Ampuero, 2009).

496

## 497 **Acknowledgements**

498

499 The author is grateful to the constructive comments provided by Ruth Harris, who suggested an  
500 important comparison with point source models, and Steve Day, who pointed out the significant  
501 contribution of a smooth velocity gradient that forms the crux of the study. The author thanks  
502 Editor Jim Kaklamanos, Kyle Withers and an anonymous reviewer for their constructive  
503 reviews. The manuscript also benefits from the comments provided by Marlon Ramos, Jing Ci  
504 Neo and Olivia Helprin. This study is supported by the National Science Foundation through  
505 Grant Award 1943742.

506

## 507 **Declaration of Competing Interests**

508

509 The authors acknowledge there are no conflicts of interest recorded.

510

## 511 **References**

512

513 Aagaard, B. T., R. W. Graves, A. Rodgers, T. M. Brocher, R. W. Simpson, D. Dreger, N. A. Petersson, S.  
514 C. Larsen, S. Ma, and R. C. Jachens (2010). Ground-motion modeling of Hayward fault scenario  
515 earthquakes, Part II: Simulation of long-period and broadband ground motions, *Bull. Seismol. Soc.*  
516 *Am.* **100**, 2945-2977.

517

518 Abercrombie, R. E. (1997). Near-surface attenuation and site effects from comparison of surface and deep  
519 borehole recordings, *Bull. Seismol. Soc. Am.* **87**, 731-744.

520

521 Ampuero, J. P. (2009). SEM2DPACK: A spectral element method tool for 2D wave propagation and  
522 earthquake source dynamics, *User's Guide*, version 2.3.6, Retrieved from [http://www.sourceforge.net/  
523 projects/sem2d/](http://www.sourceforge.net/projects/sem2d/) (last accessed October 2019).

524

525 Andrews, D. J. (1976). Rupture propagation with finite stress in antiplane strain, *J. Geophys. Res.* **81**,  
526 3575-3582.

527

528 Asano, K., H. Sekiguchi, T. Iwata, M. Yoshimi, T. Hayashida, H. Saomoto, and H. Horikawa (2016).  
529 Modelling of wave propagation and attenuation in the Osaka sedimentary basin, western Japan, during the  
530 2013 Awaji Island earthquake, *Geophys. J. Int.* **204**, 1678-1694.

531  
532 Beresnev, I. A., and K. L. Wen (1996). Nonlinear soil response—A reality?, *Bull. Seismol. Soc. Am.* **86**,  
533 1964-1978.  
534  
535 Bethmann, F., N. Deichmann, and P. M. Mai (2012). Seismic wave attenuation from borehole and surface  
536 records in the top 2.5 km beneath the city of Basel, Switzerland. *Geophys. J. Int.* **190**, 1257-1270.  
537  
538 Brocher, T. M. (2005). Empirical relations between elastic wavespeeds and density in the Earth's  
539 crust, *Bull. Seismol. Soc. Am.* **95**, 2081-2092.  
540  
541 Brocher, T. M. (2008). Compressional and shear-wave velocity versus depth relations for common rock  
542 types in northern California, *Bull. Seismol. Soc. Am.* **98**, 950-968.  
543  
544 Building Seismic Safety Council (BSSC) (2001). 2000 Edition, NEHRP Recommended Provisions for  
545 Seismic Regulations for New Buildings and Other Structures, FEMA-368, Part 1 (Provisions): developed  
546 for the Federal Emergency Management Agency, Washington, D.C.  
547  
548 Clayton, R., and B. Engquist (1977). Absorbing boundary conditions for acoustic and elastic wave  
549 equations, *Bull. Seismol. Soc. Am.* **67**, 1529-1540.  
550  
551 Dixit, A. M., A. T. Ringler, D. F. Sumy, E. S. Cochran, S. E. Hough, S. S. Martin, S. Gibbons, J. H.  
552 Luetgert, J. Galetzka, S. N. Shrestha, et al. (2015). Strong-motion observations of the M 7.8 Gorkha,  
553 Nepal, earthquake sequence and development of the N-SHAKE strong-motion network, *Seismol. Res.*  
554 *Lett.* **86**, 1533-1539.  
555  
556 Edwards, B., and D. Fäh (2013). Measurements of stress parameter and site attenuation from recordings  
557 of moderate to large earthquakes in Europe and the Middle East. *Geophys. J. Int.* **194**, 1190-1202.  
558  
559 Esmaeilzadeh, A., D. Motazedian, and J. Hunter (2019). 3D nonlinear ground-motion simulation using a  
560 Physics-based method for the Kinburn basin, *Bull. Seismol. Soc. Am.* **109**, 1282-1311.  
561  
562 Field, E. H., P. A. Johnson, I. A. Beresnev, and Y. Zeng (1997). Nonlinear ground-motion amplification  
563 by sediments during the 1994 Northridge earthquake, *Nature* **390**, 599-602.  
564  
565 Field, E.H. (2000), A modified ground motion attenuation relationship for southern California the  
566 accounts for detailed site classification and a basin depth effect, *Bull. Seism. Soc. Am.* **90**, S209-S22.  
567  
568 Frankel, A., W. Stephenson, and D. Carver (2009). Sedimentary basin effects in Seattle, Washington:  
569 Ground-motion observations and 3D simulations, *Bull. Seism. Soc. Am.* **99**, 1579-1611.  
570  
571 Graves, R. W., and A. Pitarka (2004). Broadband time history simulation using a hybrid approach. 13<sup>th</sup>  
572 World Conference on Earthquake Engineering, Vancouver, B. C., Canada, Paper No. 1098.  
573

574 Harmsen, S., S. Hartzell, and P. Liu (2008). Simulated ground motion in Santa Clara Valley, California,  
575 and vicinity from  $M \geq 6.7$  scenario earthquakes, *Bull. Seism. Soc. Am.* **98**, 1243-1271.  
576

577 Harris, R. A., M. Barall, B. Aagaard, S. Ma, D. Roten, K. Olsen, B. Duan, D. Liu, B. Luo, K. Bai, et al.  
578 (2018). A suite of exercises for verifying dynamic earthquake rupture codes, *Seismol. Res. Lett.* **89**, 1146-  
579 1162.  
580

581 Hauksson, E., and P. M. Shearer (2006). Attenuation models (QP and QS) in three dimensions of the  
582 southern California crust: Inferred fluid saturation at seismogenic depths, *J. Geophys. Res. Solid*  
583 *Earth* **111**, B05302.  
584

585 Hough, S. E., E. Thompson, G. A. Parker, R. W. Graves, K. W. Hudnut, J. Patton, T. Dawson, T.  
586 Ladinsky, M. Oskin, K. Siorattanakul, et al. (2020). Near-field ground motions from the July 2019  
587 Ridgecrest, California, earthquake sequence, *Seismol. Res. Lett.* **91**, 1542-1555.  
588

589 Huang, Y., J. P. Ampuero, and D. V. Helmberger (2014). Earthquake ruptures modulated by waves in  
590 damaged fault zones, *J. Geophys. Res. Solid Earth* **119**, 3133-3154.  
591

592 Ida, Y. (1972). Cohesive force across the tip of a longitudinal-shear crack and Griffith's specific surface  
593 energy, *J. Geophys. Res.* **77**, 3796-3805.  
594

595 Joyner, W. B., and D. M. Boore (1988). Measurement, characterization, and prediction of strong ground  
596 motion, In *Earthquake Engineering and Soil Dynamics II, Proc. Am. Soc. Civil Eng. Geotech. Eng. Div.*  
597 *Specialty Conf.* 27-30.  
598

599 Kaklamanos, J., and B. A. Bradley (2018). Challenges in predicting seismic site response with 1D  
600 analyses: Conclusions from 114 KiK-net vertical seismometer arrays, *Bull. Seism. Soc. Am.* **108**, 2816-  
601 2838.  
602

603 Kaklamanos, J., B. A. Bradley, A. N. Moolacattu, and B. M. Picard (2020). Physical hypotheses for  
604 adjusting coarse profiles and improving 1D site-response estimation assessed at 10 KiK-net sites, *Bull.*  
605 *Seism. Soc. Am.* **110**, 1338-1358.  
606

607 Kubo, H., T. Nakamura, W. Suzuki, Y. P. Dhakal, T. Kimura, T. Kunugi, N. Takahashi, and S. Aoi  
608 (2019). Ground-Motion Characteristics and Nonlinear Soil Response Observed by DONET1 Seafloor  
609 Observation Network during the 2016 Southeast Off-Mie, Japan, *Bull. Seism. Soc. Am.* **109**, 976-986.  
610

611 Ludwig, W. J. (1970). Seismic refraction, *The sea* **4**, 53-84.  
612

613 Meza-Fajardo, K. C., J. F. Semblat, S. Chaillat, and L. Lenti (2016). Seismic-wave amplification in 3D  
614 alluvial basins: 3D/1D amplification ratios from fast multipole BEM simulations, *Bull. Seism. Soc.*  
615 *Am.* **106**, 1267-1281.  
616

617 Moczo, P., J. Kristek, and L. Halada (2004). The finite-difference method for seismologists, *An*  
618 *Introduction. Comenius University, Bratislava.*

619  
620 Neighbors, C., E. J. Liao, E. S. Cochran, G. J. Funning, A. I. Chung, J. F. Lawrence, C. Christensen, M.  
621 Miller, A. Belmonte, and H. H. A. Sepulveda (2015). Investigation of the high-frequency attenuation  
622 parameter,  $\kappa$  (kappa), from aftershocks of the 2010 M w 8.8 Maule, Chile earthquake, *Geophys. J.*  
623 *Int.* **200**, 200-215.  
624  
625 Olsen, K. B. (2000). Site amplification in the Los Angeles basin from three-dimensional modeling of  
626 ground motion, *Bull. Seism. Soc. Am.* **90**, S77-S94.  
627  
628 Park, S., and S. Elrick (1998). Predictions of shear-wave velocities in southern California using surface  
629 geology, *Bull. Seism. Soc. Am.* **88**, 677-685.  
630  
631 Pitarka, A., L. A. Dalguer, S. M. Day, P. G. Somerville, and K. Dan (2009). Numerical study of ground-  
632 motion differences between buried-rupturing and surface-rupturing earthquakes, *Bull. Seism. Soc. Am.* **99**,  
633 1521-1537.  
634  
635 Pitarka, A., R. Gok, G. Yetirmishli, S. Ismayilova, and R. Mellors (2016). Ground motion modeling in the  
636 eastern caucasus. *Pure Appl. Geophys.* **173**, 2791-2801.  
637  
638 Rodgers, A. J., A. Pitarka, N. A. Petersson, B. Sjögren, and D. B. McCallen (2018). Broadband (0–4 Hz)  
639 ground motions for a magnitude 7.0 Hayward fault earthquake with three-dimensional structure and  
640 topography, *Geophys. Res. Lett.* **45**, 739-747.  
641  
642 Rodgers, A. J., A. Pitarka, R. Pankajakshan, B. Sjögren, and N. A. Petersson (2020). Regional-Scale 3D  
643 Ground-Motion Simulations of Mw 7 Earthquakes on the Hayward Fault, Northern California Resolving  
644 Frequencies 0–10 Hz and Including Site-Response Corrections, *Bull. Seism. Soc. Am.* **110**, 2862-2881.  
645  
646 Somerville, P. (2004). Differences in Earthquake Source and Strong Ground Motion Characteristics  
647 Between Shallow and Buried Faulting, In *Proceedings of OECD/NEA Workshop* (p. 5).  
648  
649 Tabor, R., and J. Bielak (2014). Ground-motion simulation and validation of the 2008 Chino Hills,  
650 California, earthquake using different velocity models, *Bull. Seism. Soc. Am.* **104**, 1876-1898.  
651  
652 Trifunac, M. D., and M. I. Todorovska (1998). Nonlinear soil response as a natural passive isolation  
653 mechanism—the 1994 Northridge, California, earthquake, *Soil Dynam. Earthq. Eng.* **17(1)**, 41-51.  
654  
655 Van Houtte, C., S. Drouet, and F. Cotton (2011). Analysis of the origins of  $\kappa$  (kappa) to compute hard  
656 rock to rock adjustment factors for GMPs, *Bull. Seism. Soc. Am.* **101**, 2926-2941.  
657  
658 Wang, Y., S. M. Day, and M. A. Denolle (2019). Geometric controls on pulse-like rupture in a dynamic  
659 model of the 2015 Gorkha earthquake, *J. Geophys. Res. Solid Earth* **124**, 1544-1568.  
660  
661 Wang, Y. J., K. F. Ma, S. K. Wu, H. J. Hsu, and W. C. Hsiao (2016). Near-Surface Attenuation and  
662 Velocity Structures in Taiwan from Wellhead and Borehole Recordings Comparisons, *TAO* **27**, 169-180.

663  
664  
665  
666  
667  
668  
669  
670  
671  
672  
673  
674  
675  
676  
677  
678  
679  
680  
681  
682

Wills, C., M. Petersen, W. Bryant, M. Reichle, G. Saucedo, S. Tan, G. Taylor, and J. Treiman (2000), A site-condition map for California based on geology and shear-wave velocity, *Bull. Seism. Soc. Am.* **90**, S187-S208.

Withers, K. B., K. B. Olsen, and S. M. Day (2015). Memory-efficient simulation of frequency-dependent Q, *Bull. Seism. Soc. Am.* **105**, 3129-3142.

Withers, K. B., K. B. Olsen, S. M. Day, and Z. Shi (2019). Ground Motion and Intraevent Variability from 3D Deterministic Broadband (0–7.5 Hz) Simulations along a Nonplanar Strike-Slip Fault Ground Motion and Intraevent Variability from 3D Deterministic Broadband Simulations, *Bull. Seism. Soc. Am.* **109**, 229-250.

**Full mailing address for each author**

Room 4534F, 1100 North University, Ann Arbor, MI 48109

**Table 1. Depth variations of  $V_p$  and  $V_s$  for simulated soil sites**

Depth $z$ (km)	$V_p$ (km/s)	$V_s$ (km/s)
$0 < z < 0.06$	$V_p = 1.711$	$V_s = 0.436$
$0.06 \leq z < 0.5$	$V_p = 1.5 + 3.735z - 3.543z^2$	$V_s = 0.7858 - 1.2344V_p + 0.7949V_p^2 - 0.1238V_p^3 + 0.0064V_p^4$
$0.5 \leq z < 4$	$V_p = 2.24 + 0.6z$	
$4 \leq z < 7$	$V_p = 4.64 + 0.3(z - 4)$	
$7 \leq z < 12$	$V_p = 5.54 + 0.06(z - 7)$	

683  
684  
685  
686  
687  
688  
689  
690  
691  
692  
693  
694  
695

**List of Figure Captions**

Figure 1. Depth variations of (a) material properties, (b) frictional parameters, and (c) fault stresses in model S. The dotted line in (a) shows the shear wave velocity in model R. Model R uses the same density, compressional wave velocity, fault friction and stresses as shown in (a), (b) and (c).

Figure 2. Comparison of (a and b) spatiotemporal distribution of slip rate, (c) slip and (d) slip rate (lowpass filtered at 4 Hz) for model S and model R.  $V_R$  in (a) and (b) gives the Rayleigh wave speed and is equal to  $0.92V_s$ . (c) and (d) show results at depths of 1, 2, 3 and 4 km from left to right.

696 Figure 3. Plots of (a-d) simulated acceleration waveforms and (e) spectra for soil and rock sites  
697 at a distance of 10 km from the fault for surface rupture. The dotted and dash-dot lines show  
698 horizontal acceleration spectra for elastic soil and rock simulations.

699 Figure 4. Plots of (a-c) simulated HVSRs and (d-f) normalized HVSRs for soil and rock sites at  
700 distances of (a and d) 5, (b and e) 10 and (c and f) 15 km from the fault for surface rupture. The  
701 dash-dot lines show results from a rock simulation with different attenuation parameters from the  
702 soil simulation, whereas the dashed lines show results from a rock simulation with the same  
703 attenuation parameters as soil.

704 Figure 5. Illustrations of (a) the depth variation of seismic wave velocities underneath soil sites  
705 for the 16-layer velocity model (solid lines) and the 5-layer velocity model (dashed lines)  
706 compared to the smooth velocity gradient (dotted and dash-dot lines), as well as (b-g) simulated  
707 HVSRs for soil and rock sites at distances of (b and e) 5, (c and f) 10 and (d and g) 15 km from  
708 the fault for the 16-layer and 5-layer velocity models (solid and dash-dot lines) compared to the  
709 simulated HVSRs for soil and rock sites in smooth velocity models (dotted lines).

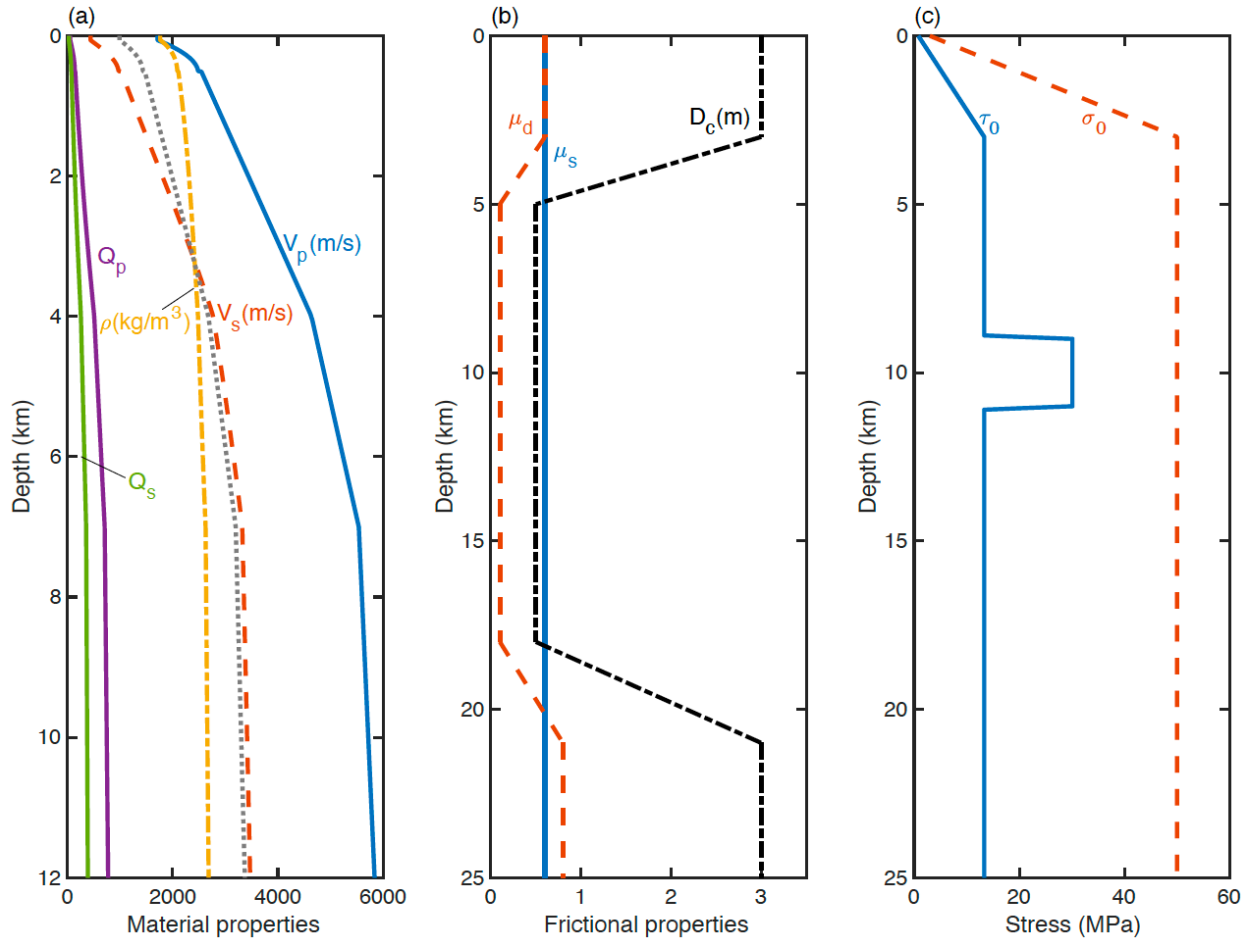
710 Figure 6. Plots of (a-d) simulated acceleration waveforms and (e) spectra for soil and rock sites  
711 at a distance of 10 km from the fault for buried rupture.

712 Figure 7. Plots of (a-c) simulated HVSRs and (d-f) normalized HVSRs for soil and rock sites at  
713 distances of (a and d) 5, (b and e) 10 and (c and f) 15 km from the fault for buried rupture.

714 Figure 8. Plots of (a-c) simulated HVSRs and (d-f) normalized HVSRs for soil and rock sites at  
715 distances of (a and d) 5, (b and e) 10 and (c and f) 15 km from the fault for a double-couple  
716 source.

717 Figure 9. Illustrations of (a) the variation of  $V_p$  (solid line),  $V_s$  (dashed line) and density (dash-  
718 dotted line) in the new soil velocity model for the top 100 m compared to the previous soil  
719 velocity model (dotted lines), as well as (b-d) simulated HVSRs and (e-g) normalized HVSRs for  
720 soil and rock sites at distances of (b and e) 5, (c and f) 10 and (d and g) 15 km from the fault.

721  
722  
723  
724  
725  
726



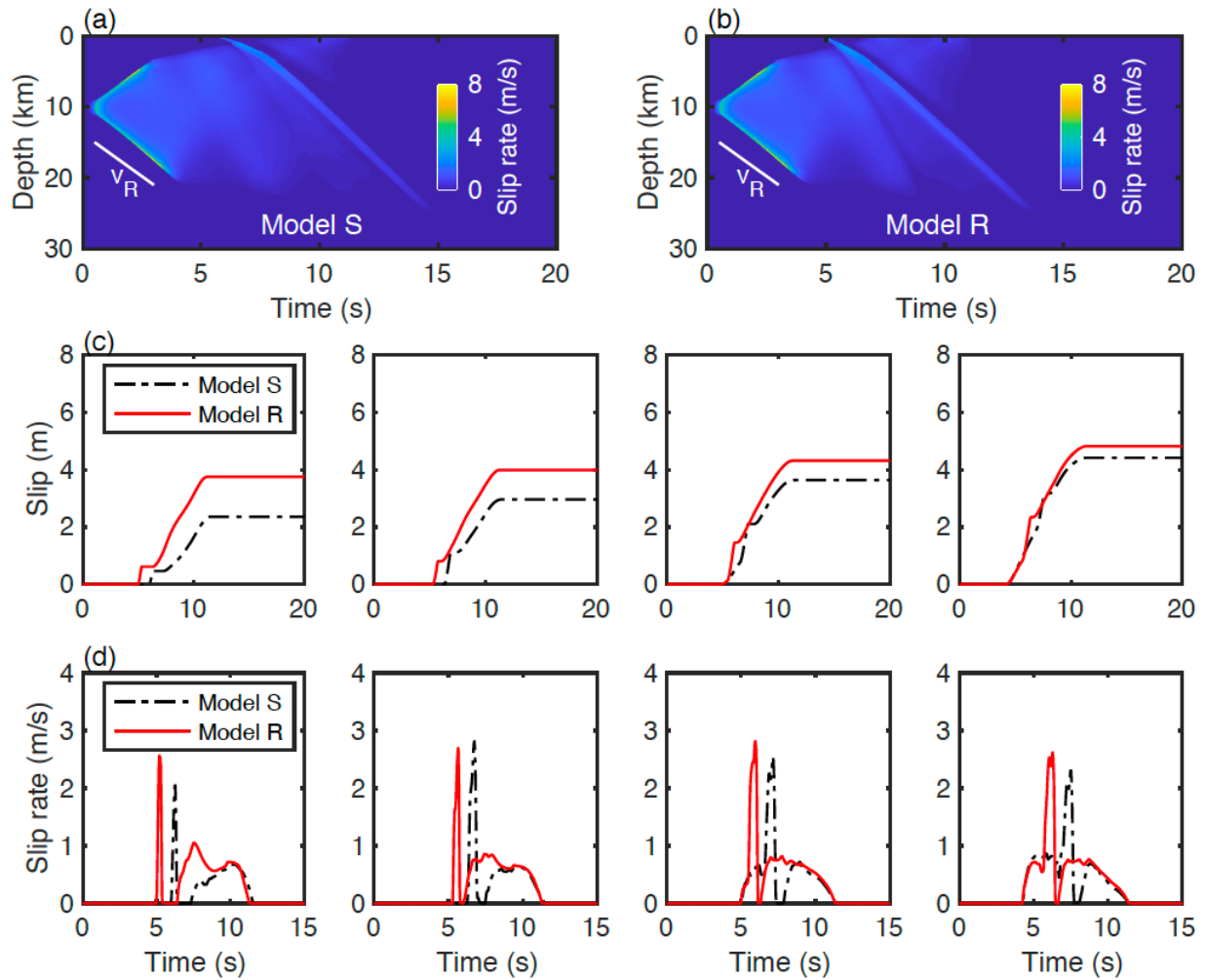
727

728

729

730

Figure 1. Depth variations of (a) material properties, (b) frictional parameters, and (c) fault stresses in model S. The dotted line in (a) shows the shear wave velocity in model R. Model R uses the same density, compressional wave velocity, fault friction and stresses as shown in (a), (b) and (c).



731

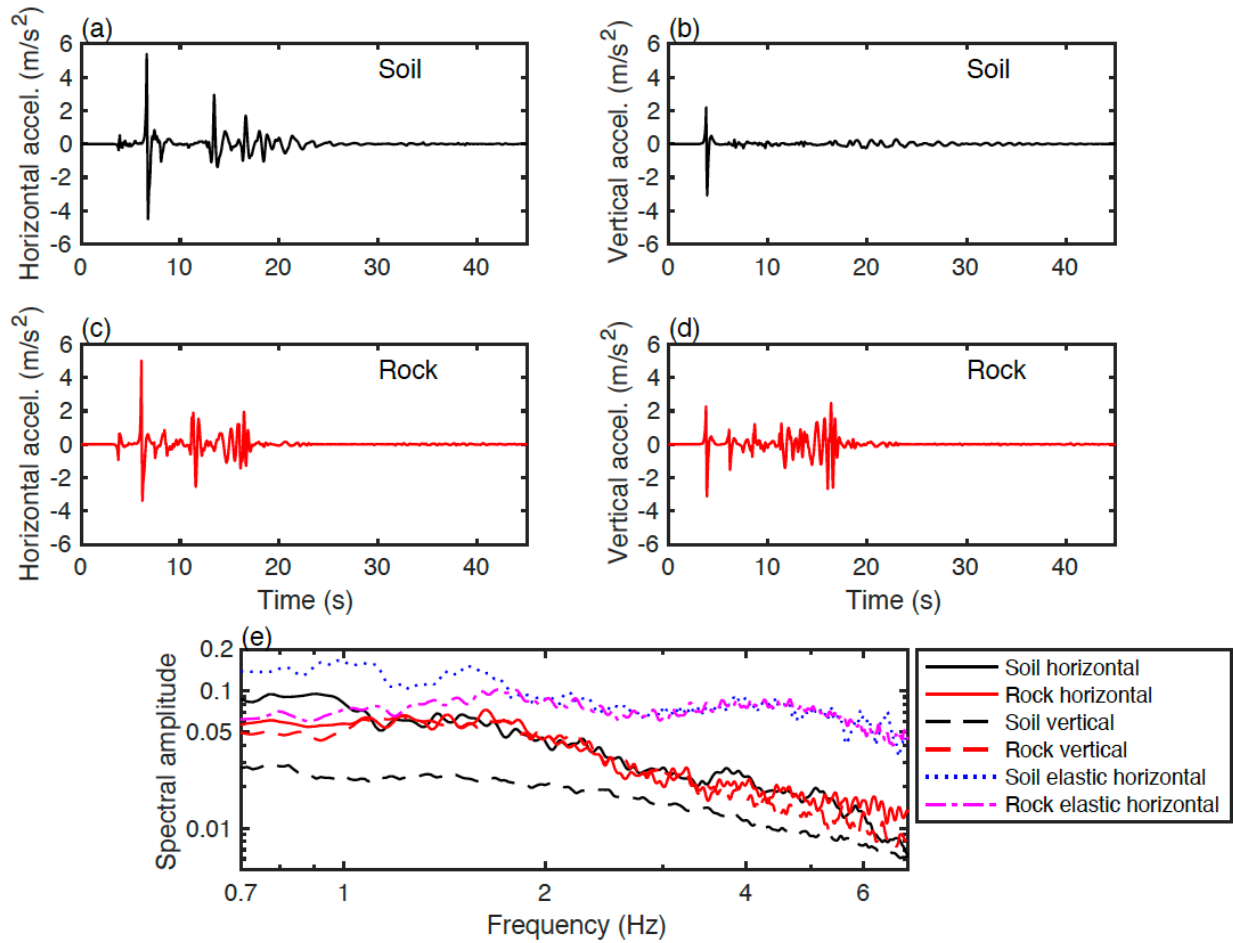
732

733

734

Figure 2. Comparison of (a and b) spatiotemporal distribution of slip rate, (c) slip and (d) slip rate (lowpass filtered at 4 Hz) for model S and model R.  $v_R$  in (a) and (b) gives the Rayleigh wave speed and is equal to  $0.92v_s$ . (c) and (d) show results at depths of 1, 2, 3 and 4 km from left to right.





735

736

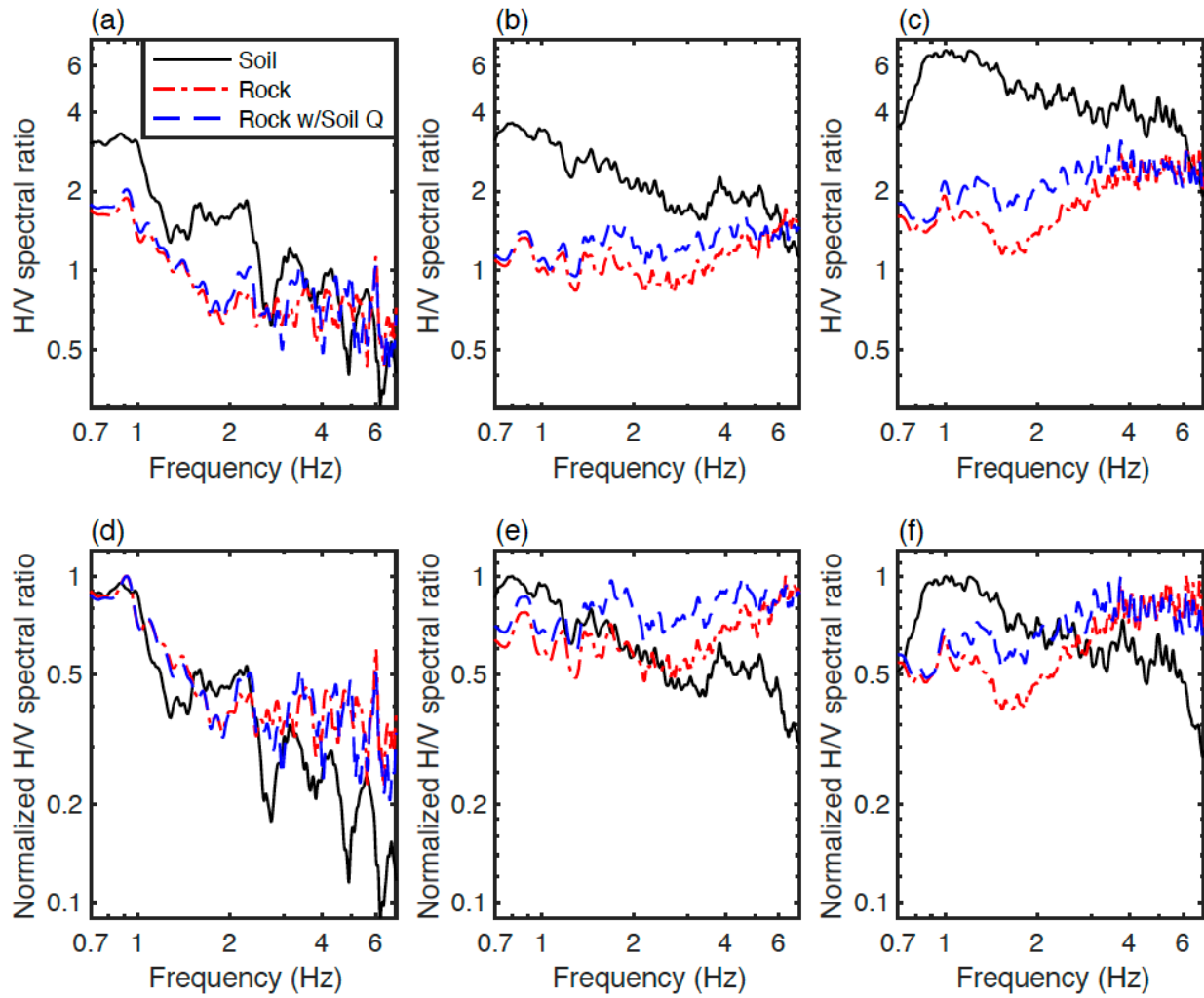
Figure 3. Plots of (a-d) simulated acceleration waveforms and (e) spectra for soil and rock sites at a

737

distance of 10 km from the fault for surface rupture. The dotted and dash-dot lines show horizontal

738

acceleration spectra for elastic soil and rock simulations.



739

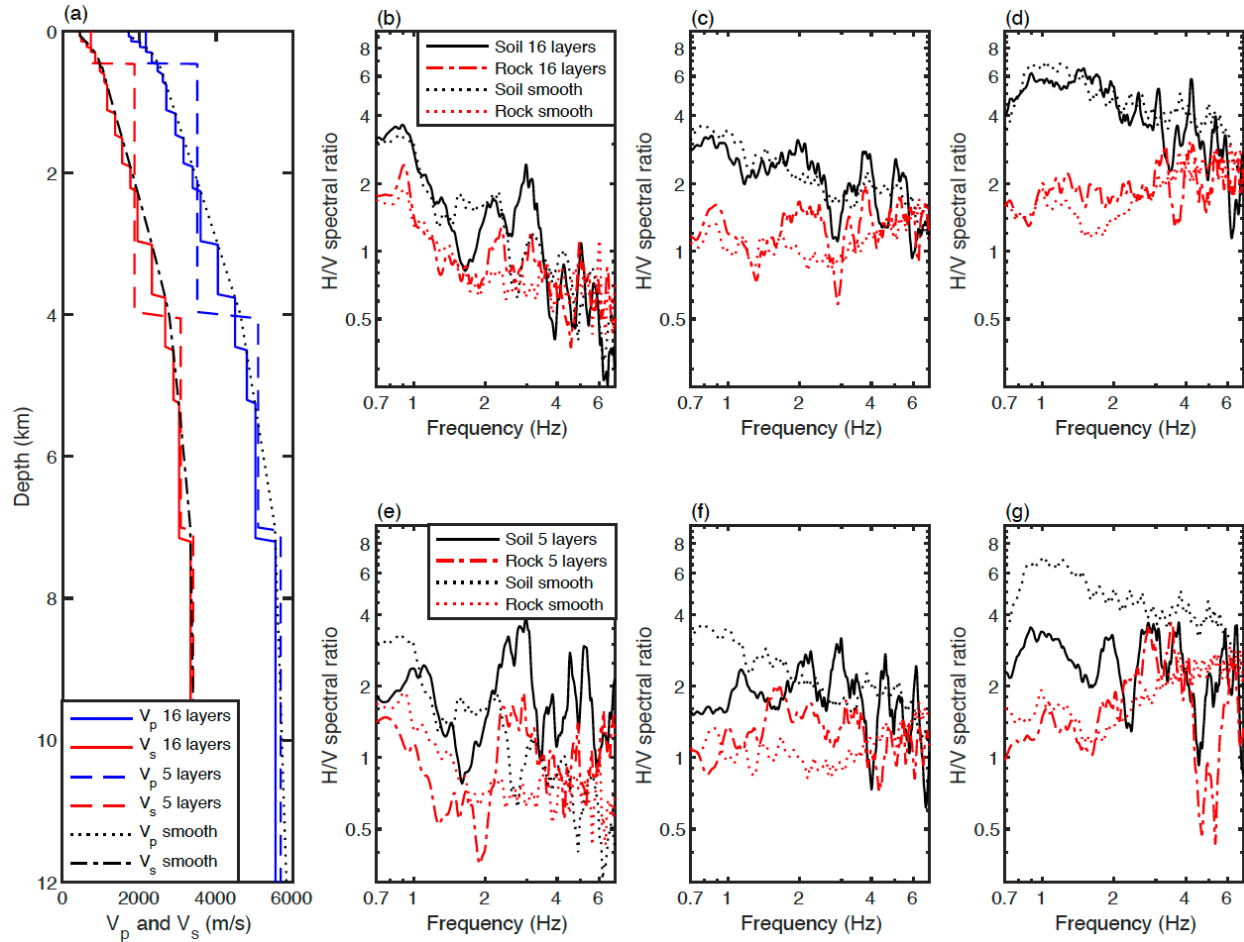
740

741

742

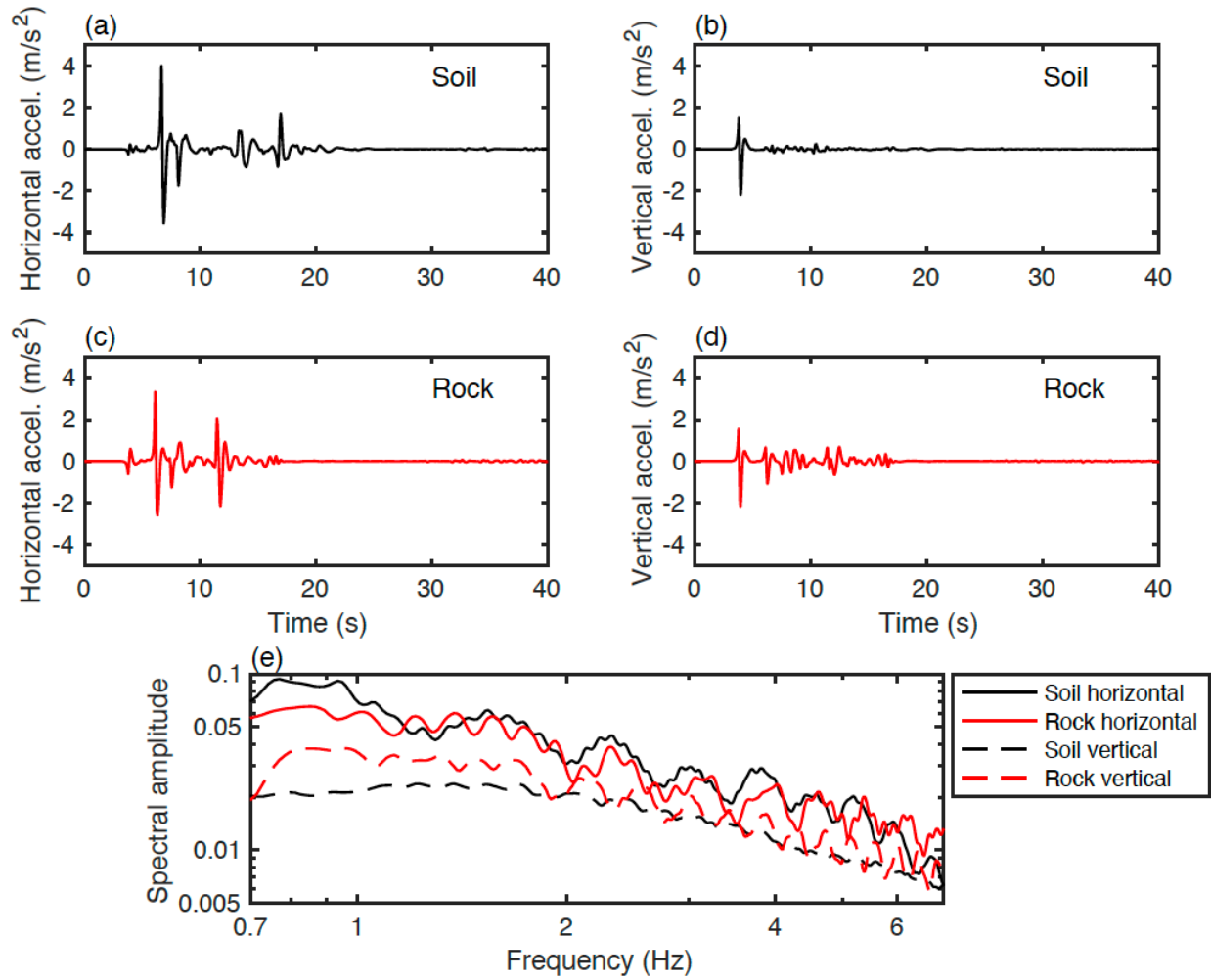
743

Figure 4. Plots of (a-c) simulated HVSRs and (d-f) normalized HVSRs for soil and rock sites at distances of (a and d) 5, (b and e) 10 and (c and f) 15 km from the fault for surface rupture. The dash-dot lines show results from a rock simulation with different attenuation parameters from the soil simulation, whereas the dashed lines show results from a rock simulation with the same attenuation parameters as soil.



744

745 Figure 5. Illustrations of (a) the depth variation of seismic wave velocities underneath soil sites for the 16-  
 746 layer velocity model (solid lines) and the 5-layer velocity model (dashed lines) compared to the smooth  
 747 velocity gradient (dotted and dash-dot lines), as well as (b-g) simulated HVSRs for soil and rock sites at  
 748 distances of (b and e) 5, (c and f) 10 and (d and g) 15 km from the fault for the 16-layer and 5-layer  
 749 velocity models (solid and dash-dot lines) compared to the simulated HVSRs for soil and rock sites in  
 750 smooth velocity models (dotted lines).



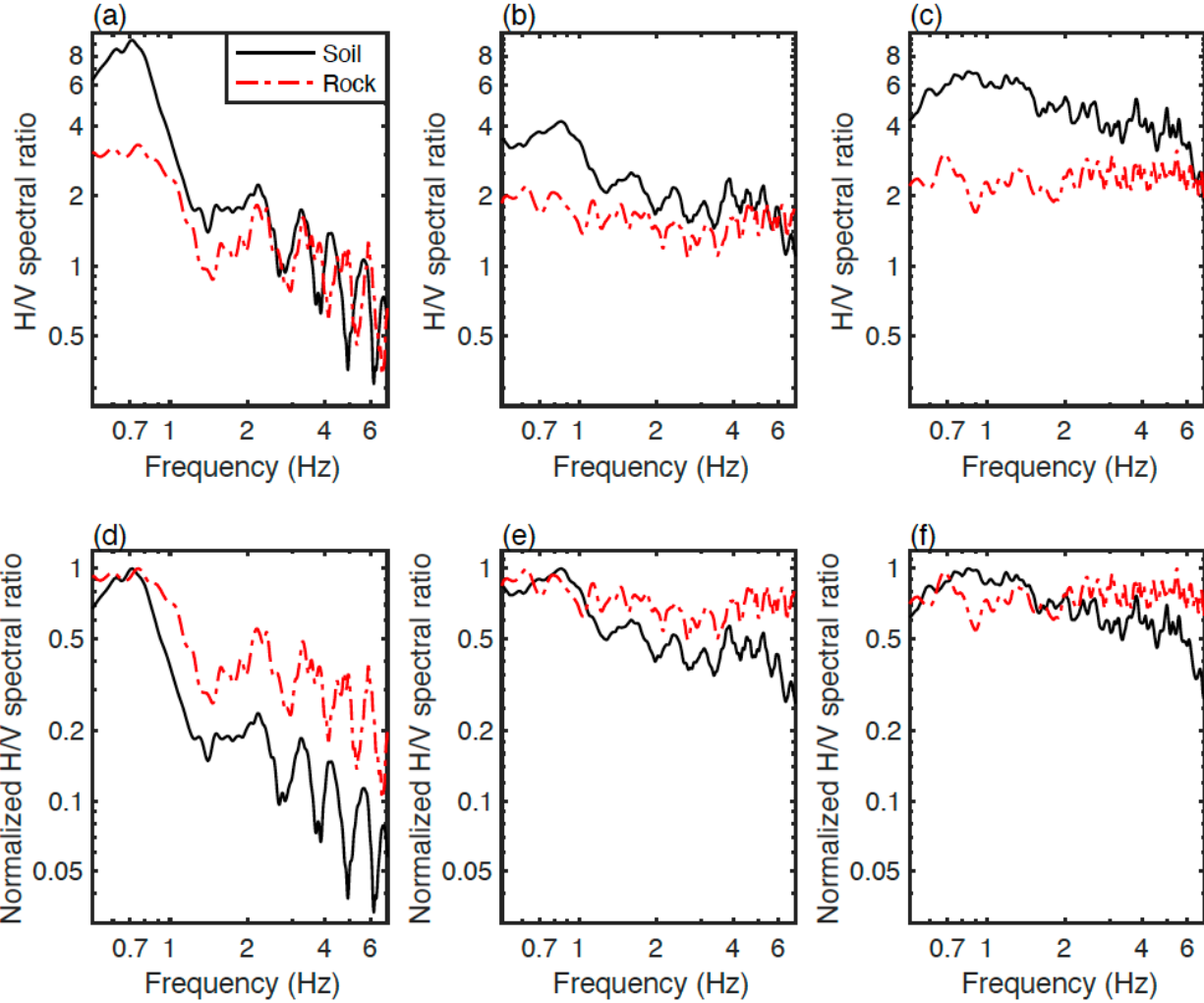
751

752 Figure 6. Plots of (a-d) simulated acceleration waveforms and (e) spectra for soil and rock sites at a

753 distance of 10 km from the fault for buried rupture.

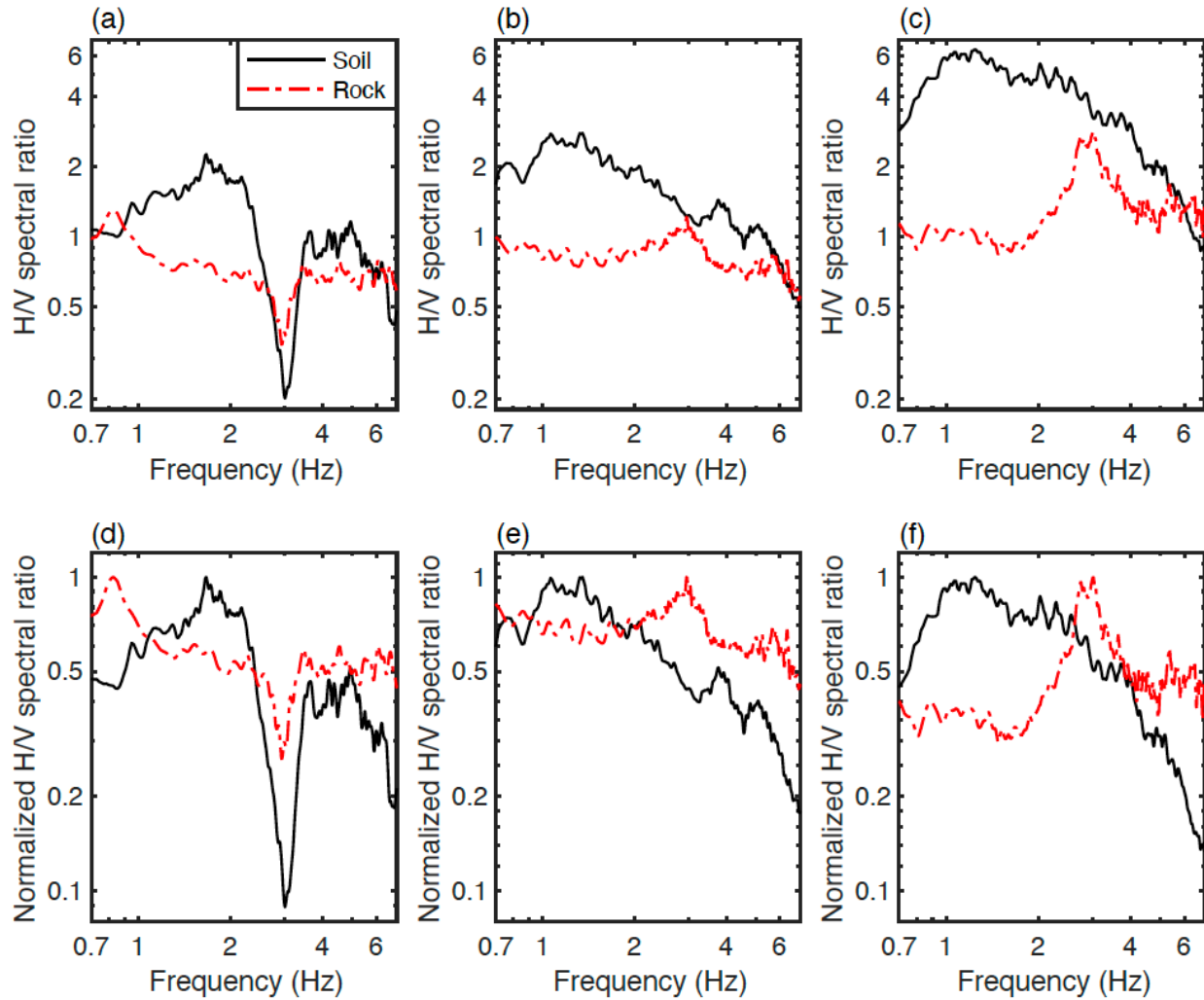
754

755



756  
 757 Figure 7. Plots of (a-c) simulated HVSRs and (d-f) normalized HVSRs for soil and rock sites at distances  
 758 of (a and d) 5, (b and e) 10 and (c and f) 15 km from the fault for buried rupture.

759  
 760



761

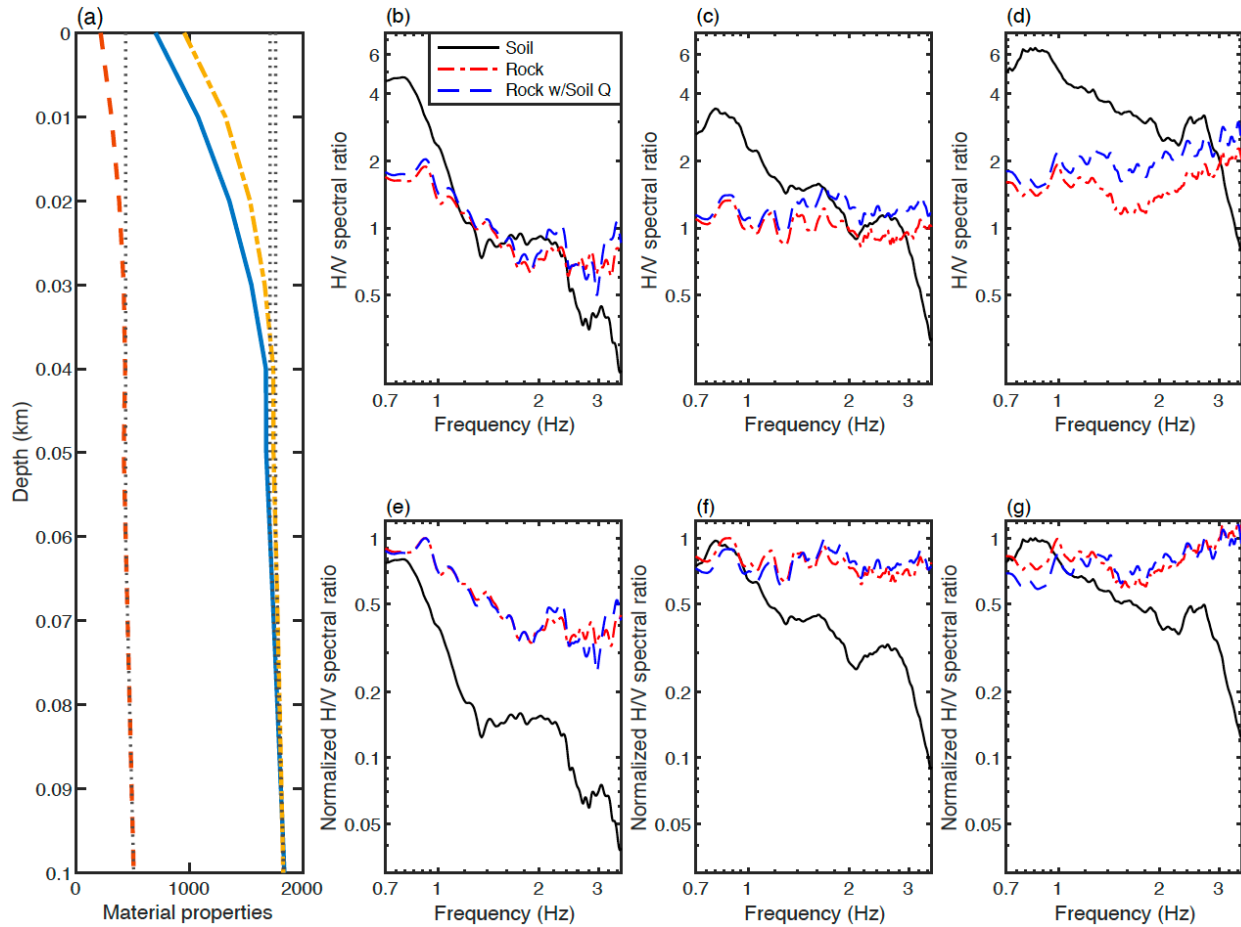
762

Figure 8. Plots of (a-c) simulated HVSRs and (d-f) normalized HVSRs for soil and rock sites at distances of (a and d) 5, (b and e) 10 and (c and f) 15 km from the fault for a double-couple point source.

763

764

765



766

767

768

769

770

Figure 9. Illustrations of (a) the variation of  $V_p$  (solid line),  $V_s$  (dashed line) and density (dash-dotted line) in the new soil velocity model for the top 100 m compared to the previous soil velocity model (dotted lines), as well as (b-d) simulated HVSRs and (e-g) normalized HVSRs for soil and rock sites at distances of (b and e) 5, (c and f) 10 and (d and g) 15 km from the fault.